ACS Catalysis

pubs.acs.org/acscatalysis Research Article

Off-Equilibrium Reactivity of Boron-Enriched Metal Diboride Surfaces in Electroreduction Conditions

Zisheng Zhang and Frank Abild-Pedersen*

Cite This: ACS Catal. 2025, 15, 12340−12350 Read Online

ACCESS | Metrics & More | Article Recommendations | Supporting Information

ABSTRACT: Boron-based materials, featuring B-dependent reactivity and diverse phases, are emerging as promising catalyst systems. However, the catalytic mechanism on many borides remains poorly understood due to complex surface reconstructions under reaction conditions. Here, we investigate the MoB_2 surface in conditions of hydrogen evolution reaction in acidic media, using grand canonical global optimization, grand canonical density functional theory, ab initio molecular dynamics, free energy surface sampling, and an analytical model for electrochemical barrier evaluation. We propose a boron-enrichment strategy to tune the surface reactivity of the hexagonal face of MoB_2. We reveal the dynamic nature of the B-enriched surface under H coverage and kinetic trapping of the system in the metastable regime with an extensive examination of the deactivation pathways. The metastable center B site on B-enriched surfaces, featuring buckled-up configuration and a usual relaxation effect, is found to be highly active toward HER via the Volmer−Heyrovsky mechanism. This work demonstrates how off-equilibrium behaviors can arise from the interplay between adsorbate coverage and surface reconstruction on a seemingly simple surface, and we present a theoretical framework and computational workflows to address these behaviors, along with other realistic complexities, in kinetics simulations.

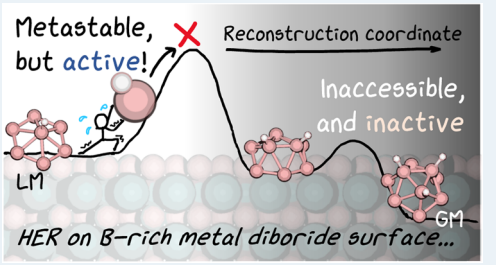

KEYWORDS: *boride, electrocatalysis, electrochemical interface, hydrogen evolution reaction, grand canonical ensemble, global optimization, surface reconstruction, kinetic trapping*

INTRODUCTION

Boron, a metalloid element with three valence electrons, is known to form unusual delocalized skeletal bonding[1] that defies the conventional view of covalency, such as the octet rule, which has been stimulating the development of modern chemical bonding theories.[2] Its unique electronic structure gives rise to great structural diversity in bulk and two-dimensional allotropes,[3,4] surface terminations,[5] as well as pure boron clusters.[6] When doped with transition metals, the boron clusters exhibit even more exotic structures and chemical bonding.[7,8] As a result, boron was considered as "arguably the most complex element in the periodic table".[9]

Such structural and electronic complexities persist in boron compounds. Metal borides, with particularly diverse stoichiometries and polymorphs, have hence emerged as a promising material system with highly tunable chemical and physical properties with broad applications, including superhardness,[10] superconductivity,[11] magnetism,[12] corrosion resistance,[13] thermoelectrics,[14] and so on.

Nonprecious transition-metal borides, meriting low cost and tunable properties, have been synthesized in nanocrystal form[15−17] and extensively tested for various electrocatalytic reactions,[18,19] as alternatives to the noble metal-based catalysts. Hydrogen evolution reaction (HER) on nonprecious metal borides,[20] in particular, exhibits intriguing boron dependency: the electrocatalytic activity depends heavily on the richness and structural arrangements of the boron content (ionic, chains, rings, graphene- and phosphene-like layers, or even cages), rather than the metal content.[21,22] The boron arrangement can be highly fluxional in some borides, inducing spontaneous disordering thermally.[23] As a result, atomistic understanding of the HER-active sites' structure and reactivity in realistic conditions has still been lacking.

The challenge in modeling boron-based catalysts lies in the strong oxygen and hydrogen affinity of boron, which results in various types of nonstoichiometric surface reconstructions during operation. Under oxidative dehydrogenation conditions, the boron content on the boride surface can get partially hydroxylated/oxidated and form an amorphous overlayer solely responsible for the catalysis,[24−27] with metal-independent reaction mechanisms.[28] Under reducing or H-rich conditions, the surface boron content can get reversibly hydrogenated to form layered hydrogen boride[29] or borophane[30] with dramatically altered chemical reactivity.[31,32] Extra boron content on the surface, as residual from synthesis,

Received: June 11, 2025
Revised: June 27, 2025
Accepted: July 1, 2025
Published: July 7, 2025

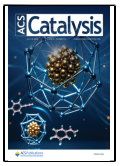

can also lead to complex and nontrivial surface reconstruction.[33,34] In electrocatalytic conditions, the system further complicates from interplay between surface restructuring, varying electrode potential, and solvent/electrolyte organization.[35−38] Hence, it is necessary to consider potential structural rearrangements, as well as the realistic aspects of the electrochemical interface under relevant conditions when studying catalysis on borides.

In this work, we revisit α-MoB_2, the most HER-active undoped nonprecious metal boride according to experimental reports.[20] Since such high activity originates in the graphene-like hexagonal layered arrangement of boron content within α-MoB_2, we focus on the boron-terminated (001) facet, the hexagonal face. Grand canonical (GC) global optimizations are performed at the density functional theory (DFT) level to sample the surface reconstruction under boron-rich or boron-deficient synthetic conditions and surface configurations under varying coverage of reaction intermediate H. Ab initio thermodynamics predicts that the B-enriched surface should undergo a major deactivating reconstruction under higher H coverages. However, computed barriers prove that the major reconstruction is kinetically unfavorable and that the surface boron would be trapped in its pristine configuration although it would become metastable thermodynamically at higher H coverages. To simulate the HER activity, we perform GC-DFT and ab initio molecular dynamics (AIMD) simulations to obtain the accessible coverage state in the HER-relevant potential window, and the coverage-dependent spatial distribution of near-surface water. We also discover strong adsorption-dependent reshaping of a specific center-atop site and how its relative time scale to HER elementary steps would influence the HER kinetics.

RESULTS AND DISCUSSION

Tunable Surface Structures through B Enrichment. In this work, we select α-MoB_2 as the parent system, as it exhibits the highest HER activity among all diboride phases. The α phase contains anionic hexagonal boron layers intercalated by layers of Mo cations in between (Figure S3). Its unique activity has been attributed to the B-terminated (001) facet,[20] which features an exposed B layer with a graphene-like honeycomb structure. The other commonly exposed facets, the armchair edge and zigzag edge, are both inactive toward HER due to overly strong binding of H (Figure S4). The common defects (B vacancy, Mo vacancy, and step edge), due to under-coordination, suffer a similar overbinding issue (Figure S4) and are also more prone to structural disintegration in reaction conditions. These are the reasons why synthetic efforts for boride catalysts have been focusing on high crystallinity instead of defect engineering.[17] For the above reasons, we focus on the B-terminated (001) facet in this study, treating it as the reference stoichiometry and referring to it as the hexagonal face hereafter.

Inspired by the great structural diversity of two-dimensional borophene and planar boron clusters, we make our first attempt to access such diversity by introducing B surplus or deficit into the hexagonal face. Experimentally, this can be achieved by controlling the amount of boron element or reagent either during the synthesis process[15] or through an extra surface treatment step on the prepared catalyst.

To account for the potential rearrangement of surface boron, we performed a global optimization minima search of the surface structure at the DFT level (Supporting Note S1). 727 unique surface phases are discovered in a wide stoichiometric range, from −1/2 to +1 monolayer (ML) of B coverage, with the structures of the global minimum (GM) surface phase of each stoichiometry shown in Figure S9. Here, the monolayer B coverage is defined with respect to the number of B_6 hexagons. By calculating the approximated grand canonical (GC) free energy with respect to B, Ω_B, of the sampled structures, we can evaluate the relative thermodynamic stability of the structures with different B coverage, μ_B

$$\Omega_B \approx E_{n_B} - E_{bare} - n_B\mu_B \quad (1)$$

Here, E, n_B, and μ_B are the electronic energy, number of extra B atoms per simulation box, and chemical potential of B, respectively, with the bare surface being the reference.

This expression allows us to establish the surface phase diagram of the MoB_2 hexagonal face as a function of μ_B. In Figure 1a, each line represents a unique surface phase, and the

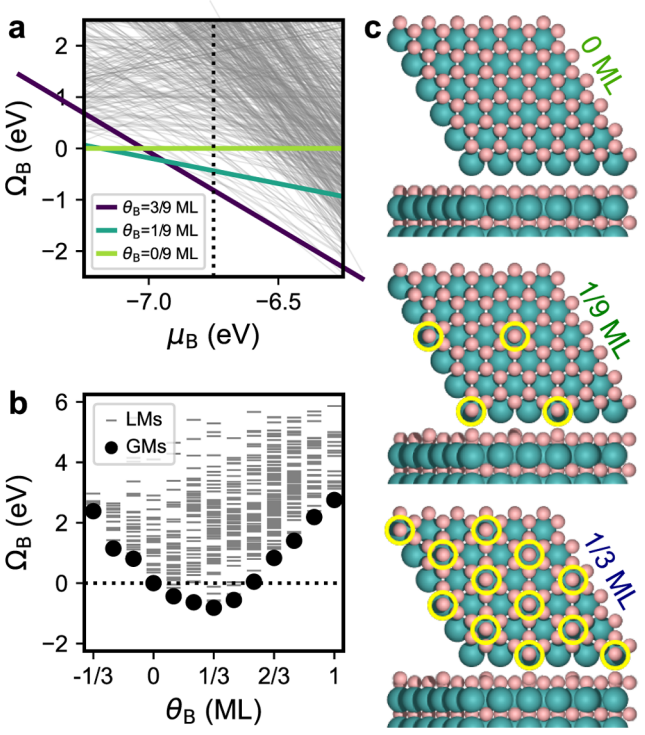

Figure 1. Ab initio thermodynamics of the boron-enriched hexagonal face of MoB_2. (a) Surface phase diagram of the MoB_2 surface with varying coverage of extra surface boron as a function of the chemical potential of B, from grand canonical global optimization sampling. The dotted line marks the chemical potential relevant to B enrichment. (b) Grand canonical free energy of the sampled surface phases with respect to B, at the chemical potential relevant to B enrichment. (c) Top and front views of the structures of the three surface phases (B_0, $B_{1/9}$, and $B_{1/3}$) that can be prepared by boron enrichment. The extra boron atoms are marked by yellow circles. Color code of atoms: Mo—blue, B—pink.

different stoichiometries lead to different responses of Ω_B to varying μ_B. To better visualize the B coverage-dependent trend of thermodynamic stability of the surface phases, we can slice the phase diagram at any specific value of μ_B, such as −6.75 eV (pure elemental boron), as in Figure 1b, revealing a stable convex hull of the GM surface phases.

Because the synthetic conditions are typically at a high temperature and there is no slow in-bulk diffusion of B

https://doi.org/10.1021/acscatal.5c04054
ACS Catal. 2025, 15, 12340−12350

involved in the surface rearrangement itself, it is safe to assume that the system can fully equilibrate and access the thermodynamically most stable surface phase during preparation. Therefore, we will focus only on the global minimum (GM) surface phase of each stoichiometry in the rest of this section. With the μ_B of pure elemental boron being the upper limit of the μ_B in the preparation process, we only consider the surface phases that can be stabilized within the range of $\mu_B < -6.75$ eV as synthetically viable. We then exclude the B-deficient surface phases due to high chemical instability of the exposed edge defects (Figure S9) and the energy penalty for breaking of the hexagonal lattice as can be seen in $\theta_B < 0$ segment of the GM convex hull in Figure 1b. This narrows our scope down to three pristine or B-enriched surface phases in Figure 1c, termed B_0, $B_{1/9}$, and $B_{1/3}$.

The hexagonal skeleton of pristine surface B_0 stays almost unchanged in all three surface phases, with the additional B content merely filling in the centers of the hexagons in a slightly buckled-up configuration. Moreover, the additional center B atoms tend to repel each other within the hexagonal B lattice instead of aggregating to form a "belt". These behaviors are quite different from the case of two-dimensional B allotropes and main-group metal diborides.[3,23] The preservation of the hexagonal skeleton on MoB_2 is likely due to the stronger interaction between B and transition metals outcompeting the fluxionality of B−B networks, leading to the dominance of the Mo lattice over the arrangement of surface B. The center B atoms, which introduce significant local strain within the surface B layer, hence tend to not stay adjacent to each other but are evenly distributed over the hexagonal lattice. The distribution of center B in $B_{1/9}$ and $B_{1/3}$ specifically matches the symmetry of the hexagonal lattice, resulting in strong stabilization as is reflected by the inaccessibility of $B_{2/9}$ in Figure 1a and the sharp bottom of the GM convex hull in Figure 1b. Experimentally, we believe that terminations with θ_B values between 1/9 and 1/3 ML should consist of a mixture of local regions of the $B_{1/9}$ and $B_{1/3}$ phases.

Reactivity of B-Enriched Surfaces under H Coverage. Having identified the three B-rich surface phases that can potentially be prepared by B-enriching treatment, we examine their electrochemical reactivity. In this work, we investigate the HER in highly acidic media (pH 0) and at a lower overpotential, where H is the only type of adsorbate, and hydronium is the primary proton source. This avoids the otherwise complication of hydroxylation (from water splitting) or borate formation in alkaline media or at oxidizing potentials (Figure S2), which we plan to address in a later study.

We first study the pristine phase B_0 to establish a reference for comparison with the other two B-enriched phases. The covalent and molecular nature of the B−H bond and the B network necessitates a nonmean-field approach to adsorbate coverage effects, i.e., explicitly finding all HER-relevant adsorption configurations. Grand canonical genetic algorithm (GCGA) is used to perform GC minima search of B_0 under varying H coverage (Supporting Note S1), with the grand canonical free energy with respect to H, Ω_H, as the search target

$$\Omega_H \approx E_{n_H} - E_{bare} - n_H\mu_H \quad (2)$$

where μ_H can be expressed as a function of reaction conditions such as pH and electrode potential U using the computational hydrogen electrode model. The δE terms denote the thermal correction terms to the free energy related to the H adsorption, including the zero point energy, constant pressure heat capacity, and vibrational entropy. The partial pressure of H_2 is assumed to be the same as the standard pressure, which corresponds to the standard experimental setup for HER testing and makes the last term zero.

$$\mu_H = \frac{1}{2}E_{H_2}^{gas} + (\delta E_H^{gas} - \delta E_H^{ads}) - \ln(10)k_BT\ pH - |e|U_{SHE} + \frac{1}{2}k_BT\ln(p/p^\circ) \quad (3)$$

In total, we sampled 1665 unique catalyst states from multiple independent GCGA searches. The H adsorption free energies, ΔG_H, of all of the GCGA-sampled catalyst states up to 1 ML H coverage are plotted in Figure 2, with notable GM structures shown below. The monolayer H coverage is defined as the highest possible H coverage without causing disintegration of the hexagonal skeleton. B_0 binds H quite strongly, with the ΔG_H ranging from −0.4 to −0.3 eV as the H coverage increases. This overbinding behavior is comparable to that of Mo and Re metals.[39]

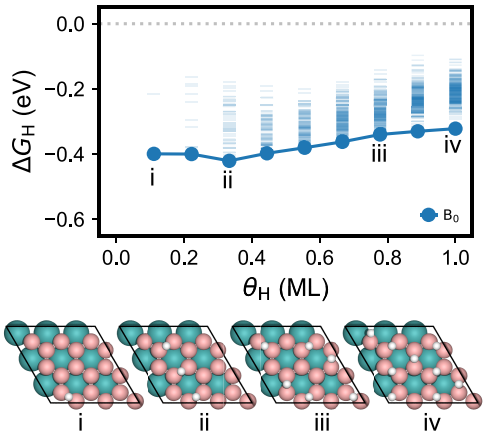

Figure 2. Adsorption free energetics of H on the pristine B_0 hexagonal face of MoB_2 under varying H coverage. The bar and circle markers represent all sampled structures and the most stable structure of each H coverage, respectively. Representative structures are shown under the plot and labeled in Roman numerals. Color code of atoms: Mo—blue, B—pink, H—white.

In the whole HER-relevant coverage regime, H always prefers to adsorb onto the bridge site (Figure S19) over the B−B edge of the hexagon units (Figure S10). This is a typical 3-center-2-electron (3c-2e) bonding mode as is characterized by the curvature of the bond path (151.7°) and a small positive Laplacian (0.016) at the bond critical point (Figure S8 and Table S1).[40] The bridge H appears as highly hydridic with a Bader charge of about −0.5 |e|, accompanying with significant electron transfer from the B that it binds to (Figure S3), and this trend persists in the whole coverage range (Figure S5). At 1/3 ML H coverage, the H adsorbates prefer to occupy the two parallel edges of the hexagons and align along a straight line. At higher coverages, they tend to spread out and adopt an alternating occupied−empty−occupied−empty pattern within each hexagon. Having two H atoms on adjacent bridge sites is highly energetically unfavorable, as the electron density on the two B atoms hosting the H is depleted (Figure S3), reducing their ability to accommodate another H. The H arrangement

https://doi.org/10.1021/acscatal.5c04054
ACS Catal. 2025, 15, 12340−12350

also has a significant symmetry stabilization effect, leading to a small spike in H adsorption strength at 1/3 and 1 ML.

For the $B_{1/9}$ phase, we conduct GCGA searches similarly, obtaining 2197 unique catalyst states in total. The ΔG_H of all of the GCGA-sampled catalyst states up to 1 ML H coverage are plotted in Figure 3, with notable GM structures shown

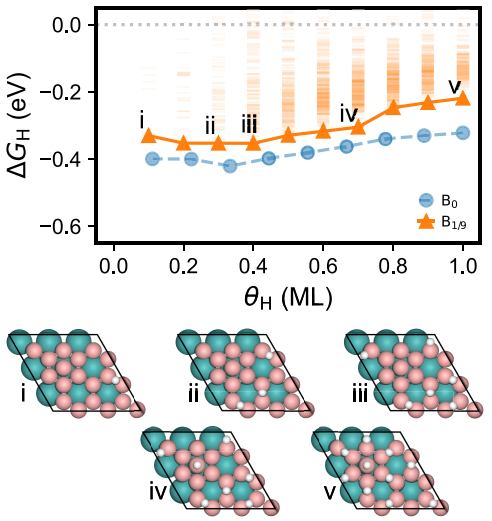

Figure 3. Adsorption free energetics of H on the $B_{1/9}$-enriched hexagonal termination of MoB_2 under varying H coverage. The bar and circle markers represent all sampled structures and the most stable structure of each H coverage, respectively. Representative structures are shown under the plot and labeled in Roman numerals. Color code of atoms: Mo—blue, B—pink, H—white.

below. Comparing to B_0, the $B_{1/9}$ phase binds H weaker by about 0.1 eV in the whole coverage range, with energetics similar to Ni and Co metals. The weakening of H binding can be attributed to the multicenter bonding formed within the B_7 unit (center B and its host B_6 unit), a typical aromatic motif, as is characterized by the strong electron delocalization above it (Figure S6). This disables the B_7 unit from forming bridge binding modes and slightly consumes the electron density within the extended conjugated system of the hexagonal layer (Figures S3 and S5), overall weakening H binding on surface B.

The center B also breaks the symmetry of the hexagonal lattice, creating a distribution of nonequivalent and nondegenerate surface sites. At low coverage, the H adsorbates prefer to occupy bridge sites that are distant from the B_7 unit (Figure S19). As H coverage increases, H continues to fill the region not adjacent to the B_7 unit, until it saturates at 2/5 ML. The next incoming H binds onto the center B in an atop σ mode, which weakens the bond between the center B and its host B_6 unit (Figure S6), leading to elevation by about 0.4 Å (Figure S18). This also partially weakens the conjugation within the B_7 (Figure S7) and activates the host B_6 unit (Figure S8 and Table S1), enabling H binding on the peripheral bridge sites of the B_7 unit at higher coverages. This leads to significant charge transfer from the center B to both its atop H and the host B_6 unit (Figure S3). Similar to the case of the B_0 phase, the H-covered $B_{1/9}$ phase exhibits a repulsive interaction among H adsorbates, with each surface B atom accommodating at most one H and each B_6 unit accommodating up to three H.

Then, we move on to the $B_{1/3}$ phase that has a higher extra surface B content, featuring alternating B_6 and B_7 units across the hexagonal lattice. Again, we performed GCGA global optimizations to search for the minima structure under varying coverage. However, this time, the searches take a much larger amount of sampling to converge, resulting in 6149 unique catalyst states in the final ensemble.

The ΔG_H of all of the GCGA-sampled catalyst states up to 1 ML H coverage are plotted in Figure 3, with notable GM structures shown below. At lower coverages, H prefers to bind atop the center B sites rather than the bridge sites as on the B_0 and $B_{1/9}$ phases (Figure S19). This change arises from the higher surface density of center B, which depletes the free valence electrons across the hexagonal lattice and deactivates the bridge B sites between the B_7 units. Furthermore, since the lattice constants are largely dictated by the MoB_2 bulk, an increased density of center B induces significant strain within the B layer. This strain leads to a greater structural buckling of the B_7 units (Figure S18), making them more susceptible to H binding. Consequently, the center-atop B*H emerges as the most favorable adsorption mode. Overall, $B_{1/3}$ still binds H weaker than the B_0 and $B_{1/9}$ phases, promising better HER thermodynamics.

However, beyond 1/4 ML coverage, the H binding gets surprisingly stronger, exhibiting a cliff-like drop in ΔG_H to about −0.5 eV. Similarly, we also observed a dramatic drop in grand canonical free energy during the GCGA search (Figure S14). This quite unphysical behavior turns out to be the result of a major surface reconstruction (Figure 4ii–iv): the center B atoms can alternatively aggregate into a B_3 trimer and reside over a B_6 unit, rearranging into a face-centered hemi-icosahedral motif. The exceptional stability of the hemi-icosahedral motif arises from the unique ability of boron to form delocalized multicenter two-electron bonds, which support three-dimensional aromaticity over a spherical frame-

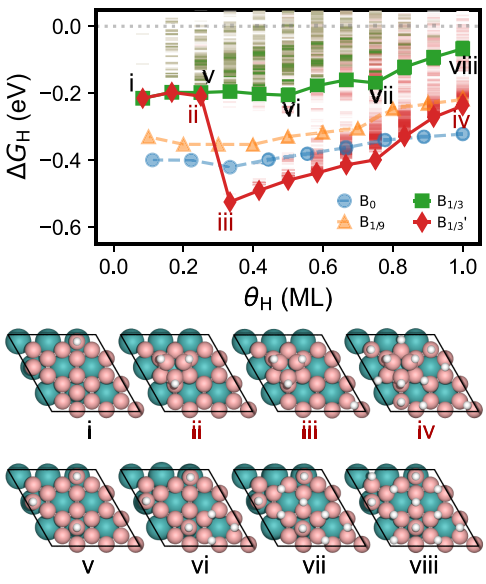

Figure 4. Adsorption free energetics of H on the $B_{1/3}$-enriched hexagonal termination of MoB_2 under varying H coverage. The bar and circle markers represent all sampled structures and the most stable structure of each H coverage, respectively. Representative structures are shown in the plot and labeled in Roman numerals. Color code of atoms: Mo—blue, B—pink, H—white.

https://doi.org/10.1021/acscatal.5c04054
ACS Catal. 2025, 15, 12340−12350

work.[41] This is also the reason why cage-like structures are prevalent in boron-rich systems, as established in elemental boron, boron clusters, and boron hydrides.[42,43] This reconstruction is only energetically competitive after all additional B atoms are capped by H. Interestingly, upon the clustering of center B*H, the freed B_6 units are activated and can afford much stronger H binding as compared to those in the unreconstructed $B_{1/3}$ phase. This makes the reconstructed phase, referred to as $B_{1/3}'$, a much worse HER electrocatalyst. In addition, the strong stabilization of H-covered B_3 trimer effectively creates a thermodynamic sink (Figure S23), trapping H indefinitely, occupying B sites, and pushing the surface further into an overbinding regime, which overall deactivates the surface for HER.

Coverage-Dependent Kinetics of Deactivation Pathways. The clustering and deactivation behavior of the extra surface B content is quite reminiscent of the sintering and ripening of nanoparticles in heterogeneous catalysis: while the thermodynamic fate of the system is to aggregate into an inactive monolith, kinetic barriers may slow down or even prevent this process. This prompted us to look into the kinetics of reconstruction.

To initiate the reconstruction, the center B atom must leave its original host B_6 unit and migrate across the surface. Initially, we consider an in-plane rearrangement mechanism, but it turns out to be kinetically unfavorable, with high barriers of about 1.5 eV (Figure S20). This is contrary to the case of MgB_2,[23] likely due to the stronger Mo−B interaction (than the mostly ionic Mg−B), which "protects" the intactness of the hexagonal lattice. Additionally, center B must migrate together with its atop H adsorbate as a single entity.

Hence, we consider a hopping mechanism, where center B hops to its adjacent B_6 unit via the shared B−B edge. To compute the activation barriers, E_a, we sample the potential energy surface (PES) of the center B hopping at varying H coverages and then locate the minimum energy path (MEP) and transition state (TS) by the string method (Supporting Note S2). The computed hopping barriers and the representative structures along the hopping coordinates are listed in Figure 5. If there is no atop H on the center B, the hopping barrier would be extremely high, at about 3 eV, making it kinetically impossible. However, just by adding an atop H onto the center B, its hopping barrier is reduced to below 1 eV. Such changes are due to the significant weakening of the B−B bond between the center B and its hist B_6 by forming an atop B−H bond, demonstrating the covalent and molecular nature of the boron layer, in stark contrast with metallic surfaces. Adding more H to the peripheral bridge sites on the surface would further lower the barrier, and the barrier reduction correlates with the H coverage. At high H coverages, the off-center B*H hopping barrier can be reduced to below 0.5 eV, which is quite viable at room temperature.

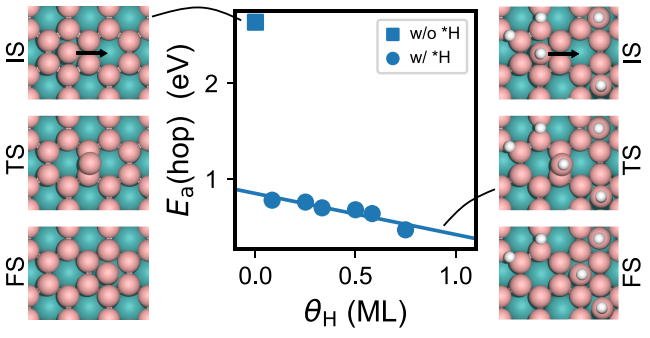

Figure 5. Activation barriers of center B hopping on the $B_{1/3}$ surface under varying H coverage. Representative structures of the initial, transition, and final states are shown next to the plot. Color code of atoms: Mo—blue, B—pink, H—white.

As the center B*H hops around, they may meet and associate over a B_6 unit. This requires a starting configuration where the two center B*H are on two adjacent B_6 units. First, we consider the process where one of the B*H (donor) migrates toward the other (acceptor) to form a dimer (Figures 6 and S27). This dimerization turns out to be neither thermodynamically nor kinetically feasible, with the barrier of about 1.25 eV in the whole coverage range. This can be rationalized by examining the TS structure: while the bridging configuration of the donor BH closely resembles that of the hopping TS, the acceptor BH must partially detach from its host B_6 unit to accommodate the donor B*H and rearrange into a B_6-supported dimer, incurring a significant energy penalty. We then consider the subsequent trimerization process, where another donor B*H migrates to associate with an adjacent dimer. Trimerization is found to be highly exothermic with a strong negative correlation between the trimerization barrier and H coverage. This trend can be attributed to the milder structural rearrangement required on the dimer side at the TS, causing the donor side to dictate the barrier. Consequently, the coverage dependences of the hopping and trimerization barriers are quite similar (facilitated by higher H coverage that weakens the B network), both decreasing to below 0.5 eV at higher H coverage. However, since dimer formation is not feasible, trimerization will not occur in the first place. As a result, the system shall be kinetically trapped in a metastable regime where center B*H species can hop around but never associate, let alone aggregate into clusters.

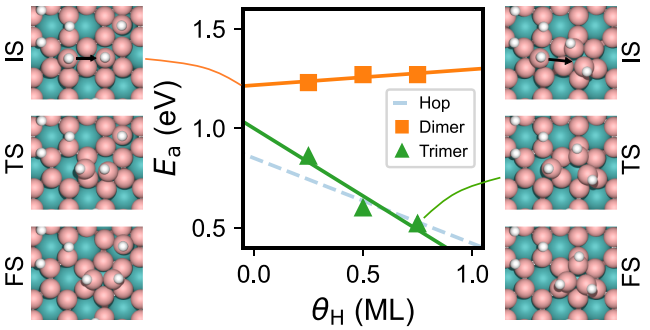

Figure 6. Activation barriers of center B dimerization and trimerization on the $B_{1/3}$ surface under varying H coverage. Representative structures of the initial, transition, and final states are shown next to the plot. Color code of atoms: Mo—blue, B—pink, H—white.

Since thermodynamics predict that the boron content decomposes into borane under acidic electroreduction conditions (Figure S2), which leads to loss of surface B content, we also compute the barriers for borane-like species formation at different H coverages (Figure 7). We find that borane can form only when a center B*H migrates toward a B−B edge with two H adsorbates on adjacent bridge sites. As the migrating B*H bridges over the B−B edge, it interacts with the two adjacent H adsorbates and uptake them to form a BH_3

https://doi.org/10.1021/acscatal.5c04054
ACS Catal. 2025, 15, 12340−12350

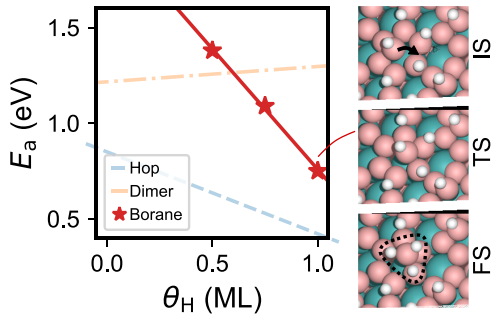

Figure 7. Activation barriers of borane formation from center B on the $B_{1/3}$ surface under varying H coverage. Representative structures of the initial, transition, and final states are shown next to the plot. Color code of atoms: Mo—blue, B—pink, H—white.

borane that can readily desorb. The borane formation barrier decreases significantly with increasing H coverage, exhibiting a strong negative correlation. At very high H coverage, the barrier is reduced to approximately 0.75 eV, which remains a relatively slow process at room temperature, and it can be mitigated by avoiding a very high overpotential to prevent excessive H coverage on the surface. We have also performed GC-DFT calculations to obtain potential-dependent electronic free energetics, shown in Figure S29. The potential-dependent variation is very small in the HER regime, and the main conclusions in this section are unchanged.

Having extensively explored potential deactivation pathways, we conclude that the system would be stranded in a thermodynamically metastable regime, undergoing significant hopping dynamics of center B*H. The aggregation of extra boron content or borane formation, despite being more thermodynamically favorable under high H coverage, is kinetically hindered. This insight prompts us to reconsider our sampling approach as described in the previous section. By design, global optimization gravitates toward the thermodynamically most stable region, potentially leading to insufficient sampling of high-lying metastable states in the case of $B_{1/3}$. To address this, we incorporated a similarity-based geometric constraint into the GCGA, biasing it away from regions corresponding to major reconstruction or borane formation (Supporting Note S1). In total, 2477 more unique catalyst states are sampled in this metastable region. The H adsorption free energies and notable structures are shown in Figure 4 (in green), which no longer has the unphysical "cliff" in ΔG_H as the $B_{1/3}'$ phase (in red). After all center B turns into B*H, the subsequent H adsorbates would all bind to the bridge site on the B_6 units until saturation. Due to the higher density of center B, H binding on bridge sites is significantly weakened, reaching a ΔG_H of approximately 0.1 eV at higher H coverages—comparable to that of Pd and Pt.

Realistic Factors and HER Activity Simulations. We have demonstrated in previous sections that the B-enriched hexagonal face of MoB_2 exhibits multiple unusual behaviors: multiple nonequivalent binding sites and modes; intricate coverage effects on energetics due to the covalent nature of the B layer; kinetic trapping and off-equilibrium evolution in the metastable regime. These complexities motivate us to go beyond thermodynamic-based activity descriptors (e.g., $|\Delta G_H|$) and mean-field microkinetic models and to consider the realistic factors into the HER activity model.

We first aim to identify the HER-relevant H coverage for B_0, $B_{1/9}$, and $B_{1/3}$ phases and how they evolve in response to varying electrode potentials. Grand canonical density functional theory (GC-DFT) calculations with polarizable implicit solvation are conducted to obtain the potential-dependent electronic grand canonical free energy, Ω_{el}, of all accessible surface states (details in Supporting Note S3). We then also treat H adsorbate grand canonically, with respect to a potential-dependent chemical potential of H, μ_H. This yields the potential-dependent total grand canonical free energy, Ω_{tot}, which allows us to compare thermodynamic stability of catalyst states with different stoichiometries and under varying electrode potentials

$$\Omega_{tot}(n_H, U) = \Omega_{el}^{n_H}(U) - \Omega_{el}^{bare}(U) - n_H\mu_H \quad (4)$$

Because the H adsorbate is found to be quite mobile over the surface, with a low diffusion barrier of about 0.2 eV (Supporting Note S4), we assume that the adsorbate configuration can sufficiently equilibrate and obey Boltzmann statistics. The population of any catalyst state i at any given electrode potential U can then be evaluated by

$$p_i(U) = \frac{e^{-\Omega_{tot,i}(U)/k_BT}}{\sum_j^N e^{-\Omega_{tot,j}(U)/k_BT}} \quad (5)$$

For the case of the $B_{1/3}$ phase, we only consider the subensemble of unreconstructed states. This approximation allows us to compute the population of every catalyst state as a function of the electrode potential (Figures 8a and S30). We can also compute the ensemble-averaged value of any property

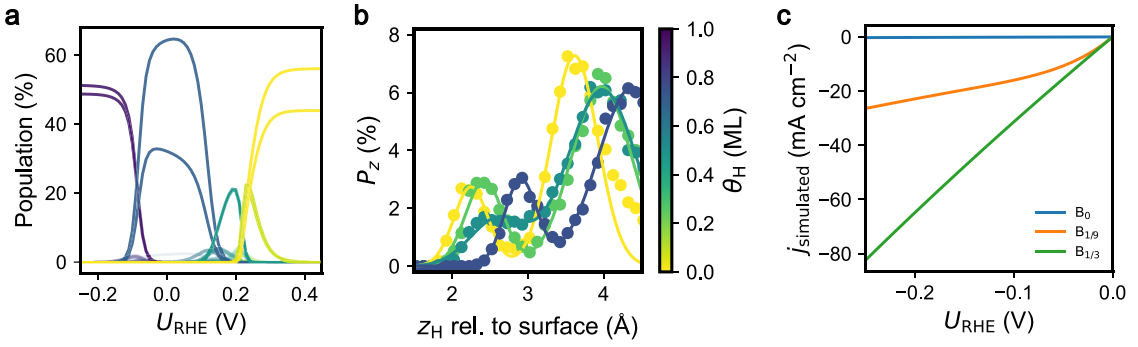

Figure 8. Kinetic simulation of hydrogen evolution reaction activity. (a) Population of catalyst states in response to varying electrode potentials on the $B_{1/3}$ phase. (b) Probability distribution of the distance between the bare pristine surface and H in water/hydronium layers on the $B_{1/3}$ phase. (c) Simulated current density on B_0, $B_{1/9}$, and $B_{1/3}$ using the multisite model.

https://doi.org/10.1021/acscatal.5c04054
ACS Catal. 2025, 15, 12340−12350

as a function of electrode potential, such as the overall H coverage

$$\langle\theta_{\mathrm{H}}\rangle = \sum_i p_i(U)\theta_{\mathrm{H},i}(U) \tag{6}$$

Across all three phases, significant underpotential deposition (UPD) of hydrogen occurs, leading to H coverages exceeding 0.5 ML at the HER onset. The H coverage continues to increase as the potential sweeps to more negative until saturation. Note that the estimation herein assumes thermodynamic equilibrium at the standard temperature and H_2 partial pressure. If H replenishment is kinetically slower than the HER, the boride surface would still retain a partial hydride state with at least 0.5 ML H coverage corresponding to the HER onset. The potential window for H UPD may be narrower, and the potential of surface H saturation may be more negative than the thermodynamic prediction. However, these kinetic effects are actually beneficial as they prevent excessive H coverage to frustrate borane formation and other H-induced deactivation. In fact, MoB_2 has been reported to maintain its activity in electrochemical cycling up to −1.0 V,[21] suggesting that most of the active sites can survive and/or the surface has its H coverage limited by HER kinetics. In either case, our main conclusions (hydride state being the active species) and the observed energetic trends (B-rich surfaces have improved HER energetics) remain unaffected.

As H coverage varies within the HER-relevant potential window, the surface gradually transforms from a flat borophene-like configuration to a corrugated borophane-like one. Such a variation in the geometry and electronic structure will induce a different distribution of the solvent and electrolyte over the surface. To account for this, we perform ab initio molecular dynamics (AIMD) simulations with explicit water and hydronium for all three phases at different H coverages accessible in the HER potential regime (Supporting Note 5). This set of simulations can explicitly capture the variation of the interfacial solvent distribution in response to the evolving surface structures induced by varying H coverage, which we will factor into kinetic modeling (vide infra). Figures 8b and S32 show the spatial distribution of hydronium H in the water/hydronium layer, P_z, as a function of distance from a pristine bare surface (z), with two apparent peaks representing the contact layer and the second water/hydronium layer. On the B_0 phase, the H in the contact layer gets closer to the surface as the H coverage increases. This counterintuitive trend is likely due to the attractive interaction between proton and the bridge H that has hydridic characters. On $B_{1/9}$, the adsorption of H on the center-atop site slightly repels the water layer away, which arises from the σ nature of the B−H bond (resembles the sterics of a typical C−H bond). On $B_{1/3}$, the repulsive effect of the center-atop H dominates the surface water/hydronium interaction. As H coverage increases, B_7 units become more buckled, strengthening the structural corrugation within the layer and pushing the center B*H higher and the contact layer further away. Since $\langle\theta_{\mathrm{H}}\rangle$ is a function of U, we can express P_z as a function of U and z for each of the surface phases.

We can then build a non-mean-field multisite model for the HER kinetics considering all afore-discussed aspects, adapted from the models proposed in refs 33,44. For each accessible catalyst state i, we compute the potential-dependent electrochemical barriers $\Delta G^{\ddagger}_{i,j}$ for every nonequivalent H adsorption site type j. The barriers are estimated analytically by constructing proton-coupled electron transfer (PCET) free energy surfaces (FESs) from the coupling of the adiabatic PESs of the H donor and acceptor (details in Supporting Note S6), following the procedures in ref 45. Note that we consider only the Volmer−Heyrovsky mechanism in the following, as the H adsorbates tend to avoid occupying adjacent sites (vide supra), making the initial configuration for the Tafel step unfavorable and resulting in prohibitively high barriers (Supporting Note S7). This behavior is in sharp contrast with metallic systems (where the Tafel step is facile and H cannot accumulate) and is supported by the experimental Tafel slope of approximately 50 mV/dec from previous studies,[20] which is characteristic of the Volmer−Heyrovsky mechanism despite highly acidic conditions. The reaction rates on site type j of catalyst state i can be calculated from the barriers and then weighed by the probability distribution P_z in Figure S32 to account for the effect of solvation fluctuation at the interface

$$r_{i,j} = \nu \int \langle\theta^{\mathrm{site}}_{i,j}(U)\rangle P_z(U, z) \mathrm{e}^{-\Delta G^{\ddagger}_{i,j}(U,z)/k_{\mathrm{B}}T}\, \mathrm{d}z \tag{7}$$

where $\theta^{\mathrm{site}}_{i,j}$ is the surface density of site type j on surface i, in units of monolayer. We can then sum up the rates over every site type for each catalyst state and then weigh them by the population of catalyst states in Figure S30 to obtain the final total rate

$$r_{\mathrm{tot}} = \sum_i p_i \left(\sum_j r_{i,j} \right) \tag{8}$$

Figure 8c shows the simulated HER current densities of the three surface phases of study. We can see that B enrichment of the surface greatly enhances HER activity. This can be attributed to multiple factors: B-enriching weakens the H binding overall and improves HER thermodynamics ($|\Delta G_{\mathrm{H}}|$ closer to zero); the corrugation of the B_7 unit under H coverage, creating center BH sites that protrude and make closer contact with the water/hydronium layer, facilitating proton transfer kinetics; compared to $B_{1/9}$, $B_{1/3}$ not only has a higher density of these center BH sites but also exhibits greater geometric corrugation due to increased strain within the surface layer caused by the crowding of more B. Since a pristine hexagonal B layer is found to be much less active for HER, we suspect that the experimentally reported high HER activity on MoB_2 and its derivatives comes from the extra boron content on the surface layer as remnants from synthetic conditions that typically involve excess boron, up to a ratio of 8:1 in B/Mo precursors used.[15] Previous experiments have also seen some activity decay after long-term cycling,[21,46] which is characteristic of the center boron species and not the pristine hexagonal lattice according to our calculations, further suggesting the presence of extra surface boron content as a key active species.

Note that, in our barrier estimations, the structure of the adsorption site is assumed to stay stationary during the PCET process; i.e., the process is nearly vertical. This has been demonstrated to be a safe and successful treatment for metallic surfaces[45] because they deform very little under H coverage and are much heavier than H, which also underlies the success of linear scaling relations for metallic surfaces.

However, it may be a different case for the surface B sites that are of light element and deform significantly upon H adsorption. Hence, we expect more fluxional behaviors, akin to what is observed on subnanometer metal clusters.[47] We probe

https://doi.org/10.1021/acscatal.5c04054
ACS Catal. 2025, 15, 12340−12350

this effect by considering two cases in which the structure of a site is allowed or forbidden to relax upon H adsorption, resulting in two adsorption free energies, ΔG_H(relax) and ΔG_H(nonrelax), respectively. The energy difference between them informs the contribution of adsorbate-induced site deformation to the overall binding energetics. In Figure 9,

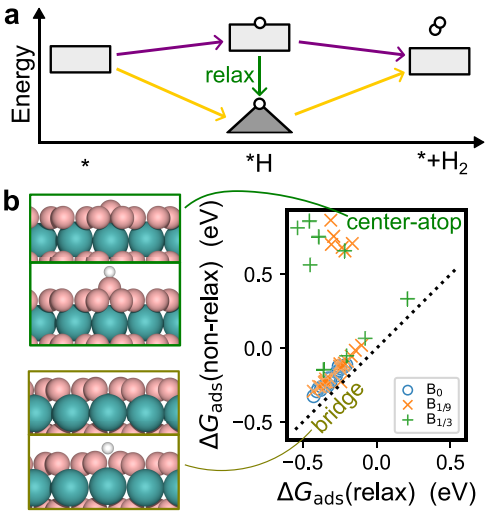

Figure 9. Site relaxation upon H adsorption and its consequences in energetics. (a) Schematic of adsorbate-induced site relaxation in the context of the hydrogen evolution reaction. (b) Adsorption free energy of H on pristine and B-enriched hexagonal surfaces of MoB_2, with or without structural relaxation of the site upon H adsorption. The two clusters of data points belong to center-atop and bridge sites, respectively, and the representative structures with and without H are shown next to the plot. Color code of atoms: Mo—blue, B—pink, H—white.

the distributions of ΔG_H(relax) of the bridge and center-atop sites are quite similar, both located around −0.3 eV. However, their ΔG_H(nonrelax) behaves very differently. For the bridge site, the effect of relaxation is negligible both energetically (less than 0.05 eV) and geometrically. For the center-atop site, however, forbidding relaxation weakens H binding significantly, by about 1 eV. When relaxation is allowed, the center B atom elevates by approximately 0.5 Å upon H binding.

This stark difference in structural and energetic changes from site relaxation arises from the distinct chemical bonding nature of the binding modes. The bridge site binds H via the 3c-2e mode, with a bonding orbital that resembles a B−B π bonding orbital in spatial distribution. As a result, the site undergoes a minimal change in structure and electron density to accommodate the H adsorbate (Figure S6). In contrast, the center-atop site binds H via the σ mode, which requires center B to free up its p_z electrons. This leads to significant electron redistribution between center B and its host B_6 (Figures S7 and S6), weakening the B−B bonds and causing center B to partially detach and pop up. The contrast again shows the intrinsic heterogeneity of sites involved on B-rich surfaces, which requires multi-site models in kinetics simulation.

Toward the end, we briefly discuss the potential implications of site relaxation in reaction kinetics. If the time scales of the site relaxation and the reaction steps are comparable, there may be some coupling between the two processes, and our nonadiabatic approximation would need correction. We tentatively probe this effect by a simple coupling scheme where the energetics of site relaxation is added to the nonadiabatic PCET FES to different extents. We found that the PCET barrier on the center-atop site can be varied by up to 1 eV at different extents of site relaxation on the center-atop site, making it behave as either over- or underbinding, i.e., either Heyrovsky- or Volmer-limited, and greatly influences the overall HER rate. The bridge site, however, is insensitive to the coupling due to lack of strong site deformation. Detailed calculations and discussions are in Supporting Note 8. Although the physical nature and tunability of this relative time scale is still unclear, we highlight the energetic span that can be potentially accessed and exploited on light-element sites with similar strong adsorption-induced deformation, which may offer new avenues in catalyst design.

CONCLUSIONS

In this work, we propose a B-enriching strategy to tune the surface reactivity of metal diborides. The arrangement of surface boron is dependent on H coverage, with a strong kinetic trapping effect to retain its initial configuration instead of drastically reconstruct or deactivate. The heterogeneity of surface sites from B-enriching, in geometry, adsorption energetics, and fluxionality, can also have a profound implication on the kinetics of relatively fast reaction steps. We emphasize the key role of off-equilibrium states and processes in catalysis and how they can emerge in seemingly simple systems. These complexities can be addressed affordably by using the generalizable computational workflow herein. The presented computational framework and the gained insights into off-equilibrium behaviors can be relevant to a wide range of catalyst and material systems, providing a new perspective in computational understanding and design.

COMPUTATIONAL METHODS

The hexagonal face of molybdenum diboride ($P6/mmm$) is modeled by a 6-layer 3 × 3 supercell of the (001) termination with a surface area of 71.581 Å^2. The bottom three atomic layers of the slab are constrained as the bulk region, and all others are allowed to relax as the interface region. A vacuum slab of 15 Å is added in the z direction to avoid spurious interactions between periodic images (Figure S1).

Density functional theory (DFT) calculations are performed with the Perdew−Burke−Ernzerhof (PBE) functional[48] and PBE_PAW pseudopotentials[49,50] (H, B, and Mo_pv) using the VASP program (version 5.4.4).[51−54] The D3 correction is added to better account for dispersion interactions.[55] The convergence criteria for electronic and force minimization are 10^{-5} eV and 2.0×10^{-2} eV/Å, respectively. The Brillouin zone is sampled using Γ-centered 2 × 2 × 1 k-points, and the kinetic energy cutoff for the plane-waves is 500 eV.

All electronic structure analyses are performed based on converged wave functions or charge densities. Electron localization functions are computed within VASP. Bader charges are computed using the Bader Charge Analysis program.[56] Quantum theory of atoms in molecules analysis is performed using the critic2 program.[57] Isosurfaces are visualized using the VESTA program.[58]

The global optimization minima searches are performed using our open-sourced Python package, GOCIA.[59] The structures of the hexagonal face with varying amounts of surface boron are sampled with an adapted version of the bond length distribution algorithm (BLDA).[60] The structures of the B_0, $B_{1/9}$, and $B_{1/3}$ surface phases under varying H coverage are

https://doi.org/10.1021/acscatal.5c04054
ACS Catal. 2025, 15, 12340−12350

sampled with the grand canonical genetic algorithm (GCGA).[35] Additional similarity constraints (full details in Supporting Note S1) are added to the sampling of unreconstructed $B_{1/3}$ under varying H coverage.

Due to the complexity of the potential energy surface (PES) of center B migration, we construct their PES from relaxed two-dimensional scan calculations (details in the SI). The minimum energy paths (MEPs) are located on the corresponding PES using the string method (Supporting Note S2).[61] The transition states of simpler processes, such as H diffusion, are located using the nudged elastic band method.[62]

The GC-DFT calculations are performed using the surface charging method[63] implemented in `GOCIA`, with details in Supporting Note S3. Only structures within 0.2 eV of the GM of their corresponding stoichiometry are considered.

Ab initio molecular dynamics simulations are performed using the same DFT methods as mentioned, except for a lower kinetic energy cutoff of 400 eV. The simulations are performed within the *NVT* ensemble at 300 K with a Nosé−Hoover thermostat.[64,65] Each simulation is run with a time step of 1 fs, and a 10 ps trajectory is collected after pre-equilibration for analysis. Full details are given in Supporting Note S5.

■ ASSOCIATED CONTENT

Data Availability Statement

All global and local minima structures from the grand canonical global optimization minima searches are available on the catalysis-hub.org repository[66] at #ZhangOff-equilibrium2025. All inputs and databases of minima searches and GC-DFT calculations are available on Zenodo repository at 10.5281/zenodo.15758067.

Supporting Information

The Supporting Information is available free of charge at https://pubs.acs.org/doi/10.1021/acscatal.5c04054.

Slab models for the GCGA, GC-DFT, and AIMD simulations; Pourbaix diagram of boron in aqueous media; Bader charge analyses; electron localization function analyses; charge density difference analysis; quantum theory of atoms in molecules analyses; global and minima structures from global optimization searches; progress plot of GCGA searches; similarity map of sampled H-covered $B_{1/3}$ structures from GCGA searches; surface atom corrugation under varying H coverage; population of different H binding sites and modes under varying H coverage; energy profiles of in-plane B rearrangement, H diffusion, and Tafel step from NEB calculations; PES of center B/B*H migration, dimerization, trimerization, and borane formation from 2D PES scans; key AIMD snapshots showing delocalization of protons in hydronium/water layers and microsolvation clusters; fitting of decoupled PES to Morse potentials; combined adiabatic FES of PCET and its response to varying U_{RHE} and ξ; note on details of the GC global optimizations; note on PES and MEP samplings; note on GC-DFT calculations; note on kinetics of H diffusion among surface sites; note on AIMD simulations; note on electrochemical barriers from decoupled PESs; and note on kinetics of the Tafel step under relevant H coverage (PDF)

■ AUTHOR INFORMATION

Corresponding Author

Frank Abild-Pedersen − *SUNCAT Center for Interface Science and Catalysis, SLAC National Accelerator Laboratory, Menlo Park, California 94025, United States;* orcid.org/0000-0002-1911-074X; Email: abild@slac.stanford.edu

Author

Zisheng Zhang − *SUNCAT Center for Interface Science and Catalysis, SLAC National Accelerator Laboratory, Menlo Park, California 94025, United States; Department of Chemical Engineering, Stanford University, Stanford, California 94305, United States*

Complete contact information is available at: https://pubs.acs.org/10.1021/acscatal.5c04054

Notes

The authors declare no competing financial interest.

■ ACKNOWLEDGMENTS

Z.Z. is supported by the Stanford Energy Fellowship from the Precourt Institute of Energy, Doerr School of Sustainability. F.A.-P. acknowledges support from the U.S. Department of Energy, Office of Science, Office of Basic Energy Sciences, Chemical Sciences, Geosciences, and Biosciences Division, Catalysis Science Program to the SUNCAT Center for Interface Science and Catalysis. Computational facilities used to conduct this study include S3DF, SLAC Shared Scientific Data Facility; Sherlock, a university-shared computing cluster operated by Stanford Research Computing Center; National Energy Research Scientific Computing Center, a DOE Office of Science User Facility supported by the Office of Science of the U.S. Department of Energy under Contract No. DE-AC02-05CH11231 using NERSC Award BES-ERCAP0024127. Z.Z. thanks Thomas F. Jaramillo, Michal Bajdich, and Kirsten Winther for helpful discussions and assistance in uploading datasets to Catalysis-Hub.

■ REFERENCES

(1) Welch, A. J. The significance and impact of Wade's rules. *Chem. Commun.* **2013**, *49*, 3615−3616.

(2) Zubarev, D. Y.; Boldyrev, A. I. "Developing paradigms of chemical bonding: adaptive natural density partitioning. *Phys. Chem. Chem. Phys.* **2008**, *10*, 5207−5217.

(3) Mannix, A. J.; Zhang, Z.; Guisinger, N. P.; Yakobson, B. I.; Hersam, M. C. Borophene as a prototype for synthetic 2D materials development. *Nat. Nanotechnol.* **2018**, *13*, 444−450.

(4) Chen, C.; Lv, H.; Zhang, P.; Zhuo, Z.; Wang, Y.; Ma, C.; Li, W.; Wang, X.; Feng, B.; Cheng, P.; et al. Synthesis of bilayer borophene. *Nat. Chem.* **2022**, *14*, 25−31.

(5) Zhou, X.-F.; Oganov, A. R.; Shao, X.; Zhu, Q.; Wang, H.-T. Unexpected reconstruction of the α-boron (111) surface. *Phys. Rev. Lett.* **2014**, *113*, No. 176101.

(6) Alexandrova, A. N.; Boldyrev, A. I.; Zhai, H.-J.; Wang, L.-S. All-boron aromatic clusters as potential new inorganic ligands and building blocks in chemistry. *Coord. Chem. Rev.* **2006**, *250*, 2811−2866.

(7) Li, W.-L.; Chen, X.; Jian, T.; Chen, T.-T.; Li, J.; Wang, L.-S. From planar boron clusters to borophenes and metalloborophenes. *Nat. Rev. Chem.* **2017**, *1*, No. 0071.

(8) Wang, L.-S. Borozenes: Benzene-like planar aromatic boron clusters. *Acc. Chem. Res.* **2024**, *57*, 2428−2436.

(9) Oganov, A. R.; Solozhenko, V. Boron: a hunt for superhard polymorphs. *J. Superhard Mater.* **2009**, *31*, 285−291.

(10) Pangilinan, L. E.; Hu, S.; Hamilton, S. G.; Tolbert, S. H.; Kaner, R. B. Hardening effects in superhard transition-metal borides. *Acc. Mater. Res.* **2022**, *3*, 100−109.
(11) Kortus, J.; Mazin, I.; Belashchenko, K. D.; Antropov, V. P.; Boyer, L. Superconductivity of metallic boron in MgB 2. *Phys. Rev. Lett.* **2001**, *86*, 4656.
(12) Scheifers, J. P.; Zhang, Y.; Fokwa, B. P. Boron: enabling exciting metal-rich structures and magnetic properties. *Acc. Chem. Res.* **2017**, *50*, 2317−2325.
(13) Zhang, J.; Liu, J.; Liao, H.; Zeng, M.; Ma, S. A review on relationship between morphology of boride of Fe-B alloys and the wear/corrosion resistant properties and mechanisms. *J. Mater. Res. Technol.* **2019**, *8*, 6308−6320.
(14) Saglik, K.; Mete, B.; Terzi, I.; Candolfi, C.; Aydemir, U. Thermoelectric borides: Review and future perspectives. *Adv. Phys. Res.* **2023**, *2*, No. 2300010.
(15) Jothi, P. R.; Yubuta, K.; Fokwa, B. P. A simple, general synthetic route toward nanoscale transition metal borides. *Adv. Mater.* **2018**, *30*, No. 1704181.
(16) Portehault, D.; Devi, S.; Beaunier, P.; Gervais, C.; Giordano, C.; Sanchez, C.; Antonietti, M. A general solution route toward metal boride nanocrystals. *Angew. Chem.* **2011**, *123*, 3320.
(17) Hong, J.; Mutalik, S.; Pescarmona, P. P.; Protesescu, L. Metal Borides: From Industrial Classics to Versatile Colloidal Nanocrystals for Energy, Catalysis, and Hard Coatings Applications. *Chem. Mater.* **2024**, *36*, 2147−2164.
(18) Gupta, S.; Patel, M. K.; Miotello, A.; Patel, N. Metal boride-based catalysts for electrochemical water-splitting: A review. *Adv. Funct. Mater.* **2020**, *30*, No. 1906481.
(19) Kawashima, K.; Márquez, R. A.; Smith, L. A.; Vaidyula, R. R.; Carrasco-Jaim, O. A.; Wang, Z.; Son, Y. J.; Cao, C. L.; Mullins, C. B. A review of transition metal boride, carbide, pnictide, and chalcogenide water oxidation electrocatalysts. *Chem. Rev.* **2023**, *123*, 12795−13208.
(20) Lee, E.; Fokwa, B. P. Nonprecious metal borides: Emerging electrocatalysts for hydrogen production. *Acc. Chem. Res.* **2022**, *55*, 56−64.
(21) Park, H.; Encinas, A.; Scheifers, J. P.; Zhang, Y.; Fokwa, B. P. Boron-dependency of molybdenum boride electrocatalysts for the hydrogen evolution reaction. *Angew. Chem., Int. Ed.* **2017**, *56*, 5575−5578.
(22) Park, H.; Zhang, Y.; Scheifers, J. P.; Jothi, P. R.; Encinas, A.; Fokwa, B. P. Graphene-and phosphorene-like boron layers with contrasting activities in highly active Mo2B4 for hydrogen evolution. *J. Am. Chem. Soc.* **2017**, *139*, 12915−12918.
(23) Li, S.; Gunda, H.; Ray, K. G.; Wong, C.-S.; Xiao, P.; Friddle, R. W.; Liu, Y.-S.; Kang, S.; Dun, C.; Sugar, J. D.; et al. Spontaneous dynamical disordering of borophenes in MgB2 and related metal borides. *Nat. Commun.* **2021**, *12*, No. 6268.
(24) Venegas, J. M.; McDermott, W. P.; Hermans, I. Serendipity in catalysis research: boron-based materials for alkane oxidative dehydrogenation. *Acc. Chem. Res.* **2018**, *51*, 2556−2564.
(25) Zhang, Z.; Jimenez-Izal, E.; Hermans, I.; Alexandrova, A. N. Dynamic phase diagram of catalytic surface of hexagonal boron nitride under conditions of oxidative dehydrogenation of propane. *J. Phys. Chem. Lett.* **2019**, *10*, 20−25.
(26) Cendejas, M. C.; Paredes Mellone, O. A.; Kurumbail, U.; Zhang, Z.; Jansen, J. H.; Ibrahim, F.; Dong, S.; Vinson, J.; Alexandrova, A. N.; Sokaras, D.; et al. Tracking Active Phase Behavior on Boron Nitride during the Oxidative Dehydrogenation of Propane Using Operando X-Ray Raman Spectroscopy. *J. Am. Chem. Soc.* **2023**, *145*, 25686−25694.
(27) Zhang, Z.; Hermans, I.; Alexandrova, A. N. Off-stoichiometric Restructuring and Sliding Dynamics of Hexagonal Boron Nitride Edges in Conditions of Oxidative Dehydrogenation of Propane. *J. Am. Chem. Soc.* **2023**, *145*, 17265−17273.
(28) Venegas, J. M.; Zhang, Z.; Agbi, T. O.; McDermott, W. P.; Alexandrova, A.; Hermans, I. Why boron nitride is such a selective catalyst for the oxidative dehydrogenation of propane. *Angew. Chem., Int. Ed.* **2020**, *59*, 16527−16535.
(29) Nishino, H.; Fujita, T.; Cuong, N. T.; Tominaka, S.; Miyauchi, M.; Iimura, S.; Hirata, A.; Umezawa, N.; Okada, S.; Nishibori, E.; et al. Formation and characterization of hydrogen boride sheets derived from MgB2 by cation exchange. *J. Am. Chem. Soc.* **2017**, *139*, 13761−13769.
(30) Li, Q.; Kolluru, V. S. C.; Rahn, M. S.; Schwenker, E.; Li, S.; Hennig, R. G.; Darancet, P.; Chan, M. K.; Hersam, M. C. Synthesis of borophane polymorphs through hydrogenation of borophene. *Science* **2021**, *371*, 1143−1148.
(31) Kawamura, R.; Cuong, N. T.; Fujita, T.; Ishibiki, R.; Hirabayashi, T.; Yamaguchi, A.; Matsuda, I.; Okada, S.; Kondo, T.; Miyauchi, M. Photoinduced hydrogen release from hydrogen boride sheets. *Nat. Commun.* **2019**, *10*, No. 4880.
(32) Rojas, K. I. M.; Cuong, N. T.; Nishino, H.; Ishibiki, R.; Ito, S.-i.; Miyauchi, M.; Fujimoto, Y.; Tominaka, S.; Okada, S.; Hosono, H.; et al. Chemical stability of hydrogen boride nanosheets in water. *Commun. Mater.* **2021**, *2*, No. 81.
(33) Zhang, Z.; Cui, Z.-H.; Jimenez-Izal, E.; Sautet, P.; Alexandrova, A. N. Hydrogen evolution on restructured B-rich WB: metastable surface states and isolated active sites. *ACS Catal.* **2020**, *10*, 13867−13877.
(34) Weng, X.-J.; Bai, J.; Hou, J.; Zhu, Y.; Wang, L.; Li, P.; Nie, A.; Xu, B.; Zhou, X.-F.; Tian, Y. Experimental evidence of surface copper boride. *Nano Res.* **2023**, *16*, 9602−9607.
(35) Zhang, Z.; Wei, Z.; Sautet, P.; Alexandrova, A. N. Hydrogen-Induced Restructuring of a Cu(100) Electrode in Electroreduction Conditions. *J. Am. Chem. Soc.* **2022**, *144*, 19284−19293.
(36) Zhang, Z.; Gee, W.; Sautet, P.; Alexandrova, A. N. H and CO Co-induced roughening of Cu surface in CO2 electroreduction conditions. *J. Am. Chem. Soc.* **2024**, *146*, 16119−16127.
(37) Shah, A. H.; Zhang, Z.; Wan, C.; Wang, S.; Zhang, A.; Wang, L.; Alexandrova, A. N.; Huang, Y.; Duan, X. Platinum Surface Water Orientation Dictates Hydrogen Evolution Reaction Kinetics in Alkaline Media. *J. Am. Chem. Soc.* **2024**, *146*, 9623−9630.
(38) Zhang, Z.; Li, J.; Wang, Y.-G. Modeling Interfacial Dynamics on Single Atom Electrocatalysts: Explicit Solvation and Potential Dependence. *Acc. Chem. Res.* **2024**, *57*, 198−207.
(39) Nørskov, J. K.; Bligaard, T.; Logadottir, A.; Kitchin, J.; Chen, J. G.; Pandelov, S.; Stimming, U. Trends in the exchange current for hydrogen evolution. *J. Electrochem. Soc.* **2005**, *152*, J23.
(40) Kalita, A. J.; Rohman, S. S.; Kashyap, C.; Ullah, S. S.; Reza, S.; Borah, B.; Guha, A. K. Multicenter bonding in s-block metals: An insight from theory. *Comput. Theor. Chem.* **2019**, *1167*, No. 112606.
(41) Poater, J.; Escayola, S.; Poater, A.; Teixidor, F.; Ottosson, H.; Viñas, C.; Solà, M. Single- Not Double- 3D-Aromaticity in an Oxidized Closo Icosahedral Dodecaiodo-Dodecaborate Cluster. *J. Am. Chem. Soc.* **2023**, *145*, 22527−22538.
(42) Kettle, S. F. A.; Tomlinson, V. The electronic structure of the boron hydrides. Part I. Cage molecules. *J. Chem. Soc. A* **1969**, 2002−2006.
(43) Zhai, H.-J.; Kiran, B.; Li, J.; Wang, L.-S. Hydrocarbon analogues of boron clusters—planarity, aromaticity and antiaromaticity. *Nat. Mater.* **2003**, *2*, 827−833.
(44) Zhang, Z.; Masubuchi, T.; Sautet, P.; Anderson, S. L.; Alexandrova, A. N. Hydrogen Evolution on Electrode-Supported Ptn Clusters: Ensemble of Hydride States Governs the Size Dependent Reactivity. *Angew. Chem.* **2023**, *135*, No. e202218210.
(45) Li, J.; Stenlid, J. H.; Ludwig, T.; Lamoureux, P. S.; Abild-Pedersen, F. Modeling potential-dependent electrochemical activation barriers: revisiting the alkaline hydrogen evolution reaction. *J. Am. Chem. Soc.* **2021**, *143*, 19341−19355.
(46) Jothi, P. R.; Zhang, Y.; Scheifers, J. P.; Park, H.; Fokwa, B. P. T. Molybdenum diboride nanoparticles as a highly efficient electrocatalyst for the hydrogen evolution reaction. *Sustainable Energy Fuels* **2017**, *1*, 1928−1934.
(47) Yan, G.; Vlachos, D. G. Impact of Metal Clusters on the Lewis Acidity of Oxide Surfaces: First-Principles Calculations of Pt10/γ-Al2O3 (110). *J. Phys. Chem. C* **2024**, *128*, 16996−17005.

https://doi.org/10.1021/acscatal.5c04054
ACS Catal. 2025, 15, 12340−12350

(48) Perdew, J. P.; Burke, K.; Ernzerhof, M. Generalized gradient approximation made simple. *Phys. Rev. Lett.* **1996**, *77*, 3865.
(49) Kresse, G.; Joubert, D. From ultrasoft pseudopotentials to the projector augmented-wave method. *Phys. Rev. B* **1999**, *59*, 1758.
(50) Blöchl, P. E. Projector augmented-wave method. *Phys. Rev. B* **1994**, *50*, No. 17953.
(51) Kresse, G.; Hafner, J. Ab initio molecular dynamics for liquid metals. *Phys. Rev. B* **1993**, *47*, 558−561.
(52) Kresse, G.; Hafner, J. Ab initio molecular-dynamics simulation of the liquid-metal-amorphous-semiconductor transition in germanium. *Phys. Rev. B* **1994**, *49*, 14251−14269.
(53) Kresse, G.; Furthmüller, J. Efficient iterative schemes for ab initio total-energy calculations using a plane-wave basis set. *Phys. Rev. B* **1996**, *54*, 11169−11186.
(54) Kresse, G.; Furthmüller, J. Efficiency of ab-initio total energy calculations for metals and semiconductors using a plane-wave basis set. *Comput. Mater. Sci.* **1996**, *6*, 15−50.
(55) Grimme, S.; Antony, J.; Ehrlich, S.; Krieg, H. A consistent and accurate ab initio parametrization of density functional dispersion correction (DFT-D) for the 94 elements H-Pu. *J. Chem. Phys.* **2010**, *132*, No. 154104.
(56) Yu, M.; Trinkle, D. R. Accurate and efficient algorithm for Bader charge integration. *J. Chem. Phys.* **2011**, *134*, No. 064111.
(57) Otero-de-la Roza, A.; Johnson, E. R.; Luaña, V. Critic2: A program for real-space analysis of quantum chemical interactions in solids. *Comput. Phys. Commun.* **2014**, *185*, 1007−1018.
(58) Momma, K.; Izumi, F. VESTA 3 for three-dimensional visualization of crystal, volumetric and morphology data. *Appl. Crystallogr.* **2011**, *44*, 1272−1276.
(59) Zhang, Z.; Gee, W.; Lavroff, R. H.; Alexandrova, A. N. GOCIA: a grand canonical global optimizer for clusters, interfaces, and adsorbates. *Phys. Chem. Chem. Phys.* **2025**, *27*, 696−706.
(60) Zhai, H.; Alexandrova, A. N. Local fluxionality of surface-deposited cluster catalysts: The case of Pt7 on Al2O3. *J. Phys. Chem. Lett.* **2018**, *9*, 1696−1702.
(61) Weinan, E.; Ren, W.; Vanden-Eijnden, E. String method for the study of rare events. *Phys. Rev. B* **2002**, *66*, No. 052301.
(62) Mills, G.; Jónsson, H.; Schenter, G. K. Reversible work transition state theory: application to dissociative adsorption of hydrogen. *Surf. Sci.* **1995**, *324*, 305−337.
(63) Steinmann, S. N.; Sautet, P. Assessing a First-Principles Model of an Electrochemical Interface by Comparison with Experiment. *J. Phys. Chem. C* **2016**, *120*, 5619−5623.
(64) Nosé, S. Constant temperature molecular dynamics methods. *Prog. Theor. Phys. Suppl.* **1991**, *103*, 1−46.
(65) Hoover, W. G. Canonical dynamics: Equilibrium phase-space distributions. *Phys. Rev. A* **1985**, *31*, 1695.
(66) Winther, K. T.; Hoffmann, M. J.; Boes, J. R.; Mamun, O.; Bajdich, M.; Bligaard, T. Catalysis-Hub. org, an open electronic structure database for surface reactions. *Sci. Data* **2019**, *6*, No. 75.

https://doi.org/10.1021/acscatal.5c04054
ACS Catal. 2025, 15, 12340−12350